

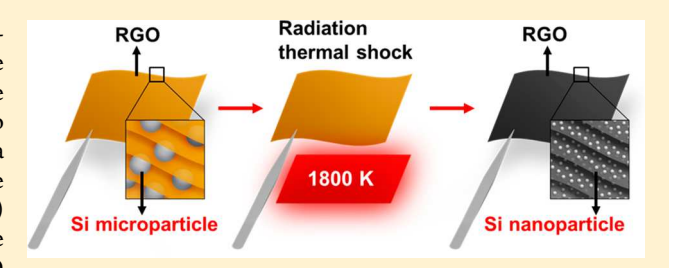
Rapid, in Situ Synthesis of High Capacity Battery Anodes through High Temperature Radiation-Based Thermal Shock

Yanan Chen, Yiju Li, Yanbin Wang, Kun Fu, Valencia A. Danner, Jiaqi Dai, Steven D. Lacey, Yonggang Yao, and Liangbing Hu*

Department of Materials Science and Engineering, University of Maryland, College Park, Maryland 20742, United States

Supporting Information

ABSTRACT: High capacity battery electrodes require nanosized components to avoid pulverization associated with volume changes during the charge-discharge process. Additionally, these nanosized electrodes need an electronically conductive matrix to facilitate electron transport. Here, for the first time, we report a rapid thermal shock process using high-temperature radiative heating to fabricate a conductive reduced graphene oxide (RGO) composite with silicon nanoparticles. Silicon (Si) particles on the order of a few micrometers are initially embedded in the RGO



host and in situ transformed into 10-15 nm nanoparticles in less than a minute through radiative heating. The as-prepared composites of ultrafine Si nanoparticles embedded in a RGO matrix show great performance as a Li-ion battery (LIB) anode. The in situ nanoparticle synthesis method can also be adopted for other high capacity battery anode materials including tin (Sn) and aluminum (Al). This method for synthesizing high capacity anodes in a RGO matrix can be envisioned for roll-to-roll nanomanufacturing due to the ease and scalability of this high-temperature radiative heating process.

KEYWORDS: Rapid manufacturing, Li-ion batteries, high-capacity anodes, reduced graphene oxide, roll-to-roll

ithium-ion batteries (LIBs) are particularly important for ✓ future electronics and electric vehicles due to their high energy density and long cycle life. To further increase the energy density of LIBs, scientists are investigating a range of high-capacity electrode materials including silicon (Si), tin (Sn), aluminum (Al), and lithium (Li) metal as anodes as well as sulfur (S) and oxygen as cathode materials. $^{1-10}$ Additionally, effective electron transport is required in electrode designs to facilitate the charge-discharge process. In this case, active electrode materials are often mixed with highly conductive carbon materials such as carbon black, carbon nanotubes, and reduced graphene oxide (RGO). However, these highcapacity composite anodes suffer from volume changes during lithiation and delithiation which degrade electrochemical performance.^{8,21-24} Nanostructures can effectively overcome this challenge as previously demonstrated with nanowires, nanoparticles, core—shell nanofibers, and hollow structures, among others. 25-30 These structural designs have been successfully demonstrated for Si, Sn, Al, S, and so forth. 4,27,28,31,32 Low-cost, high-speed manufacturing of these nanostructures is important for practical technology adoption, and yet, a rapid and scalable nanomanufacturing process remains elusive. 33,34 Moreover, due to the high surface area of nanostructures, agglomeration is another major challenge when assembling nanowires or nanoparticles into a functional electrode.2

In this study, we report a rapid, one-step, in situ synthesis method to transform microparticles into ultrafine nanoparticles (~15 nm in diameter) embedded in a conductive RGO matrix through a high-temperature radiation-based thermal shock procedure. To illustrate this method, commercial Si microparticles (SiMPs) within a RGO host (RGO-SiMPs) undergo a thermal shock treatment to create uniformly dispersed Si nanoparticles (SiNPs) in a conductive RGO matrix (RGO-SiNPs). The approach can be implemented for a range of highcapacity battery electrode materials, such as Sn and Al hosted in RGO, due to the high broadband absorption of RGO nanosheets. Additionally, the in situ synthesized nanoparticles are well-dispersed in the RGO matrix and do not agglomerate which is favorable for battery applications.

As shown in Figure 1, a freestanding RGO film with embedded SiMPs is fabricated with a simple filtration process accompanied by a prethermal reduction. The freestanding RGO-SiMPs film is placed on top of a high temperature heater or any other commercial heating element. In this way, the solution-based RGO paper can act as a planar radiation heater be heated to a high temperature by Joule heating and tuned by the applied input power. The RGO-SiMPs film is then radiation heated by the RGO paper underneath for 30 s. SiMPs are in situ transformed into SiNPs which are well-dispersed inside the highly conductive RGO matrix. We also used exactly the same approach to synthesize Sn nanoparticles and Al nanoparticles in a conductive matrix directly. All of these high-capacity LIB anode particles are well-dispersed in the conductive RGO

Received: May 24, 2016 Revised: August 3, 2016 Published: August 9, 2016



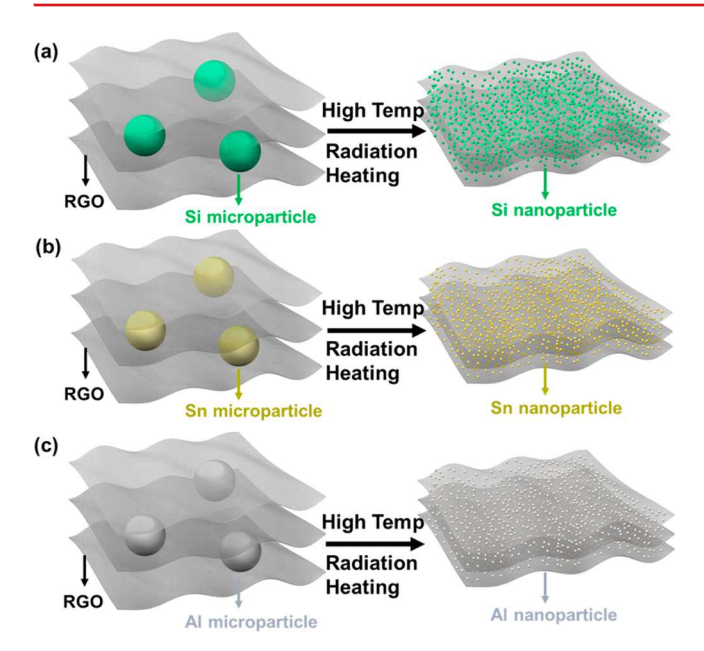


Figure 1. Schematic illustrating a new nanoparticle (NP) synthesis methodology used for battery applications. (a) Pristine SiMPs ($\sim\!2~\mu m$) within RGO are transformed into SiNPs ($\sim\!10~nm$) by a thermal shock treatment at $\sim\!1800$ K for 30 s. The methodology also can be used to synthesize other anode composites with (b) Sn and (c) Al. The shortest radiative heating time required to transform microparticles to nanoparticles is $\sim\!1~s$, which is validated using the Sn microparticle RGO films.

matrix, which can be used directly for high-performance batteries.

Figure 2a shows the setup for rapid, in situ synthesis of RGO-SiNPs from RGO-SiMPs via a high-temperature radiation-based thermal shock treatment. Typically, a suspended RGO paper was used as the radiative heating source. The electrical

current applied induced a high temperature source for nanoparticle synthesis and thermal reduction.^{39–41} The RGO-SiMPs film was prepared by vacuum filtrating a GO-SiMPs solution followed by a 1 h prereduction at 573 K in an Ar-filled tube furnace (Figure 2b, details in Supporting Information). The RGO-SiMPs film can be rapidly heated to a high temperature when placed on top of the hot RGO paper (middle image in Figure 2a) due to the high absorption coefficient of the RGO nanosheets (similar behavior as graphene).42 The RGO-SiMPs film possessed a high optical absorption of 70-86% from 2500 to 200 nm (Figure 2c). which indicates the excellent heat absorption capability using the proposed high temperature radiation process. After a short duration, the RGO-SiMPs film was moved away from the hot RGO paper to cool the film down to room temperature. To quantify the RGO paper temperature, a spectrometer-coupled optical fiber was employed. This fiber was placed above the RGO paper to detect and record the emission spectra of the RGO paper at different current values (Figure S1 in Supporting Information). The corresponding temperature was obtained using the emission spectra in a wavelength range of 340-950 nm (Figure 2d) and fitting the spectra to the blackbody radiation equation (solid black curves shown in Figure 2d). The spectral radiance significantly enhances with increasing electrical current, indicating a higher temperature. Based on the temperature-power curve, the fitted temperature increases in a nearly linear manner with increasing electrical power (Figure 2e). For instance, the temperature increases from 1250 to 1800 K when the input power changes from 0.2 to 0.7 W. Note that, when a small current (100 mA) was applied to the RGO paper, a high temperature of 1800 K was obtained, which corresponds to the bright light shown in the inset of Figure 2e. The fine tuning of the RGO heating temperature allows us to study the appropriate temperature needed to synthesize the nanoparticles hosted in a RGO matrix.

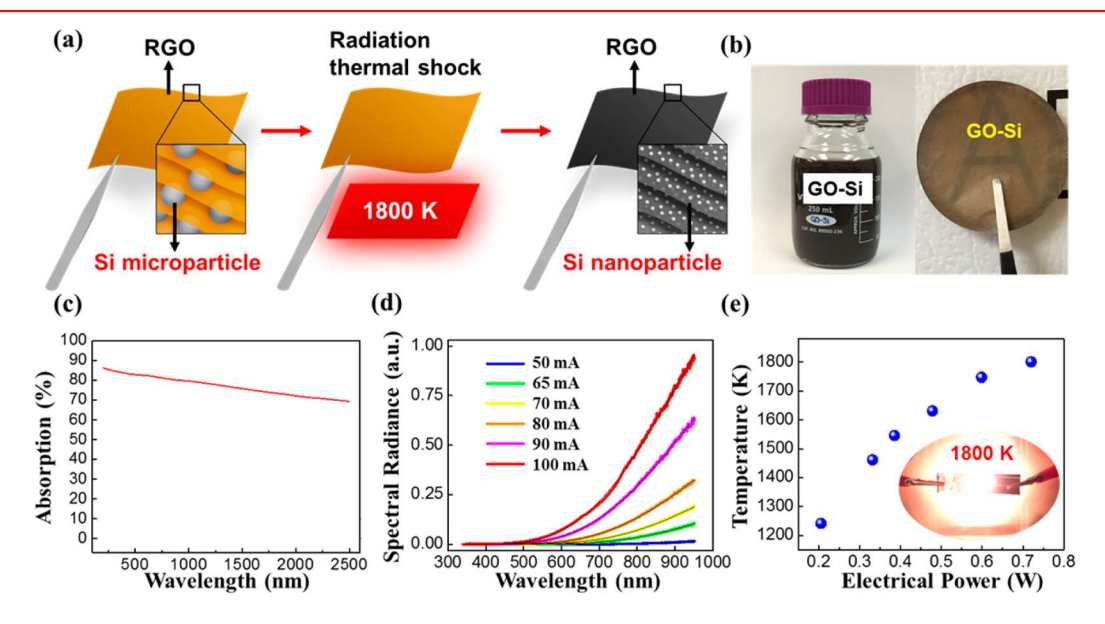


Figure 2. (a) Homemade setup for synthesizing anode nanoparticle composites. RGO-SiMPs (left image) can be rapidly transformed into RGO-SiNPs (right image) after being placed on top of the hot RGO paper (middle image). (b) Digital images of the GO-SiMPs solution and the asprepared GO-SiMPs film. (c) Optical absorption measurements of the RGO-SiMPs film, exhibiting a high absorption of 70–86% in the wavelength range of 200–2500 nm. (d) Spectral radiance measurements of RGO paper at different electrical power inputs. The temperature is determined by fitting the spectra to Planck's law assuming constant emissivity (solid black curves). (e) Fitted temperature as a function of the input electrical power for RGO paper. Inset is the illuminated RGO paper radiating due to the high temperature (1800 K) induced by an applied electrical current.

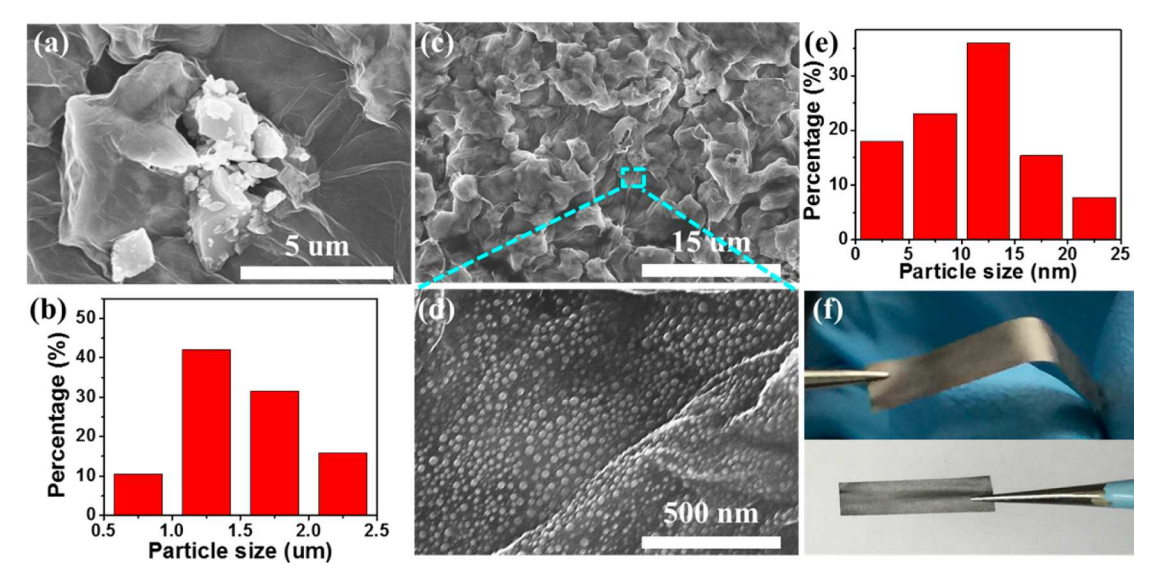


Figure 3. (a) An SEM image of the RGO-SiMPs film. (b) Statistical particle size distribution (PSD) of SiMPs in a RGO network before thermal shock treatment. (c, d) SEM images of RGO-SiNPs film after a 30 s thermal shock treatment at ~1800 K. (e) PSD of SiNPs in a RGO network after thermal shock. (f) Digital images exhibiting the flexibility of the RGO-SiNPs film after thermal shock.

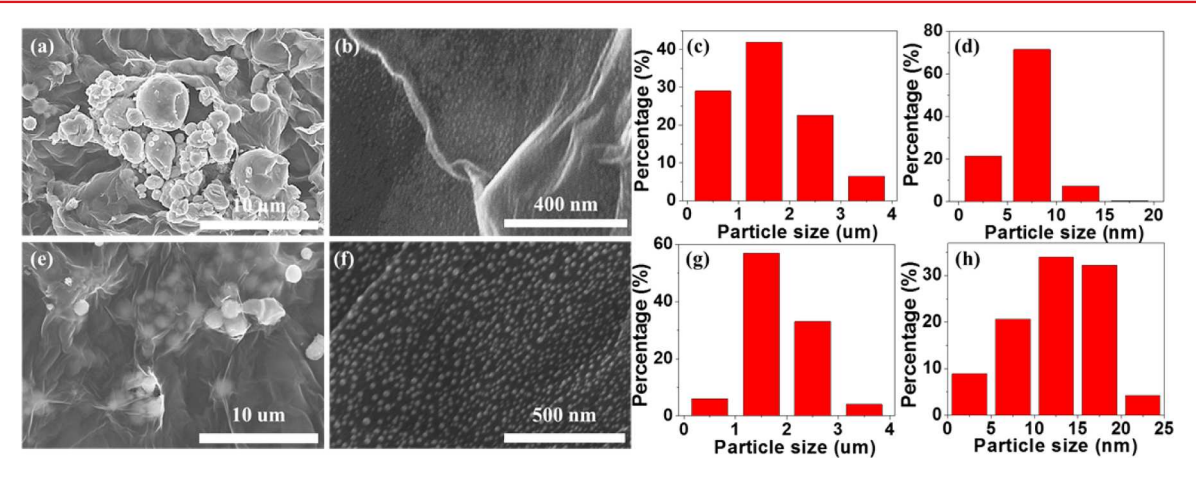


Figure 4. (a, b) SEM images of a RGO-SnMPs film and a RGO-SnNPs film after a 30 s thermal shock treatment at \sim 1550 K, respectively. (c, d) PSD of SnMPs and SnNPs. (e, f) SEM images of a RGO-AlMPs film and a RGO-AlNPs film after a 30 s thermal shock treatment at \sim 1700 K, respectively. (g, h) PSD of AlMPs and AlNPs.

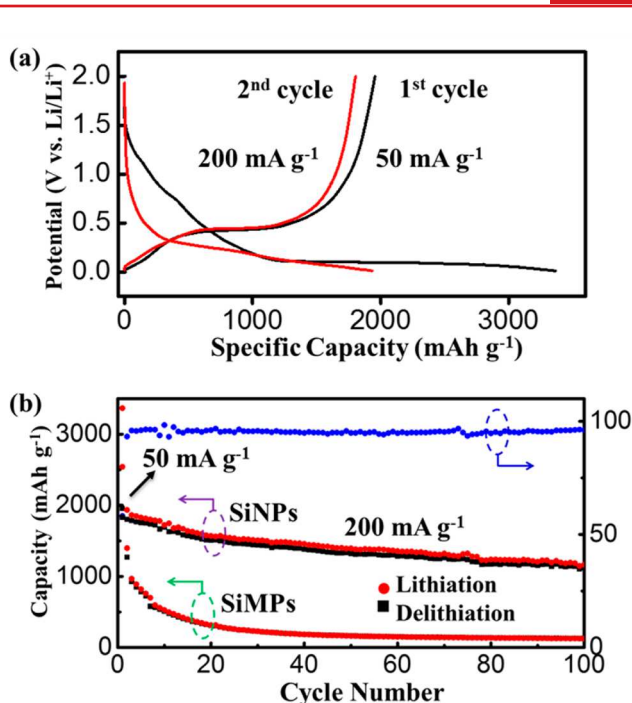
To investigate the morphological change of the RGO-SiMPs film before and after thermal shock treatment, scanning electron microscopy (SEM) measurements were carried out. The typical morphology of a RGO-SiMPs film is shown in Figure 3a, revealing that randomly aggregated, crumpled RGO nanosheets are closely associated with irregular SiMPs. The original SiMPs have a wide size distribution from 0.5 to 2.5 μm with an average diameter of 1.5 μ m (Figure 3b). After a 30 s thermal shock treatment of the RGO-SiMPs film at ~1800 K, the RGO-SiNP film is formed. Figure 3c and d show typical SEM images of evenly distributed SiNPs inside the RGO matrix. As a result of the thermal shock treatment, the SiMPs are transformed into SiNPs, which have a small size distribution predominantly between 10 and 15 nm (Figure 3e). To determine the morphological changes in more detail, additional SEM images of the pristine SiMPs and SiNPs are provided in Figure S2 (Supporting Information). The proposed transformation mechanism from SiMPs to SiNPs during the thermal shock treatment of the RGO-SiMPs film is as follows. The SiMPs melt into liquid Si due to the thermal radiation and

distribute throughout the entire RGO matrix. The melted liquid Si is trapped in the RGO due to the defects on RGO nanosheets, and upon cooling, the melted Si nucleates, precipitates, and self-assembles into ultrafine SiNPs that evenly distribute across the entire RGO surface. X-ray diffraction (XRD) of the as-prepared RGO-SiNPs film shows sharp Si peaks and a broad RGO peak, indicating the high crystallinity of the SiNPs (Figure S3a, Supporting Information). Raman spectroscopy (Figure S3b, Supporting Information) also confirms that the designed nanoarchitecture contains RGO and pure SiNPs without silicon carbides. The lack of silicon carbide formation is due to the thermal shock temperature remaining below the formation temperature of silicon carbides. Note that silicon carbide can be detected from Raman spectroscopy when the thermal shock temperature increased to ~1900 K (Figure S4), which reveals a suitable SiNPs synthesis temperature is <1900 K. Thermogravimetric analysis (TGA) shows that the SiNPs content of the RGO-SiNPs film is around 39 wt % (Figure S3c, Supporting Information). Note that the as-obtained RGO-SiNPs film exhibits excellent

flexibility and mechanical strength since the film can be bent reversibly (Figure 3f).

The method we developed for rapidly synthesizing SiNPs can be applied to a broad range of materials, including semiconductors or metals. Here, Sn and Al nanoparticle-based films are also fabricated to verify the general methodology. The morphology of pristine Sn microparticles within the RGO (RGO-SnMPs) film is shown in Figure 4a. The microscopy images reveal that spherical Sn microparticles are enclosed in wrinkled and randomly stacked RGO nanosheets similar to the RGO-SiMPs film. After a 30s thermal shock treatment at ~1550 K, a copious amount of Sn nanoparticles (SnNPs) are obtained and distributed evenly inside the RGO nanosheets (Figure 4b and Figure S5). The dimensions of the Sn particles vary from 2 μ m to 7 nm using statistical particle size distribution (PSD) analysis (Figure 4c, d). Furthermore, we find that the dimensions of the synthesized nanoparticles are controllable by changing the experimental conditions, such as the holding time of the thermal shocking process. For example, the particle size increased to approximately 50 nm at a prolonged hold time of 1 h at ~1550 K (Figures S6-S7, Supporting Information), which is likely due to agglomeration of the small nanoparticles. Similar to Si and Sn, Al can be readily transformed from microsize (Figure 4e) to nanosize (Figure 4f) particles using the thermal shock method at \sim 1700 K for 30 s. After the thermal shock treatment, Al microparticles (AlMPs) with an average diameter of 2 μ m (Figure 4g) disappeared, and Al nanoparticles (AlNPs) with an average diameter of 13 nm (Figure 4h) were evenly distributed on the RGO nanosheets. Additional microscopy images are shown in Figures S8 and S9 to compare the size variation of Al particles.

To demonstrate the thermally shocked nanoparticle composites as high-capacity LIB anodes, the RGO composite films were placed in coin cells and acted as a freestanding, carbon/binder-free electrode. The electrochemical performance of the RGO-SiNPs film was elucidated by galvanostatic discharge-charge measurements. Figure 5a shows the discharge-charge curves of the RGO-SiNPs anode for the first two cycles. The cell was cycled with a potential window of 0.01 to 2.0 V (vs Li/Li⁺) at a current density of 50 mA g⁻¹. In the initial discharge cycle, the potential maintains a long flat plateau at around 0.1 V and then gradually decreases to 0.01 V. This corresponds to Li insertion into crystalline Si, causing the formation of an amorphous Li_xSi phase. 43,44 The first charge curve displays a plateau at 0.42 V, which corresponds to the delithiation process. Subsequent discharge and charge curves show characteristic voltage profiles of Si which is consistent with previous studies. 45,46 The overall discharge and charge capacities for the first cycle are 3367 mA h g⁻¹ and 1957 mA h g⁻¹, respectively, corresponding to an initial Coulombic efficiency of 58%. The initial Coulombic efficiency can be improved by compositing controlled amount of molten Li into the RGO/nanoparticles composites to compensate the Li loss in the first cycle. The RGO-SiNPs can deliver a volumetric capacity of 3543 mA h cm⁻³ with an areal capacity of 2.48 mA h cm⁻² at 0.13 mA cm⁻². The capacity retention of the RGO-SiNPs electrode was studied at 200 mA g⁻¹ (Figure 5b) between 0.01 and 2.0 V. Note that the capacity decreased to 1165 mA h g^{-1} over 100 cycles, which is ascribed to a small capacity decay of 0.40% per cycle. Conversely, the RGO-SiMPs film delivered a small charge capacity of 126 mA h g⁻¹ over 100 cycles with a severe capacity loss of 0.95% per cycle. The excellent cycling performance of the RGO-SiNPs film is due to



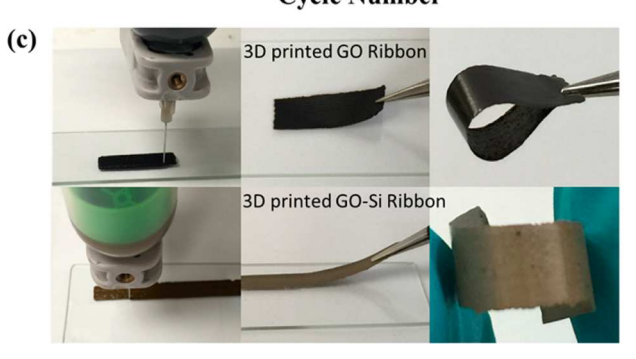


Figure 5. (a) Galvanostatic discharge/charge profiles of the RGO-SiNPs film for the first and second cycle. These tests were conducted in the potential range of $0.01-2.0~\rm V~\rm s~\rm Li/Li^+$ at 50 mA g $^{-1}$ and 200 mA g $^{-1}$, respectively. (b) Cycling performance of the RGO-SiNPs and RGO-SiMPs films at 200 mA g $^{-1}$ with the first cycle tested at 50 mA g $^{-1}$. (c) Left: Digital images showing the GO and GO-Si ribbons being 3D printed. Middle: Digital images showing that 3D printed ribbons can be peeled off from the substrate. Right: Digital images exhibiting the flexibility of the 3D printed ribbons.

the ultrafine SiNPs and the RGO matrix reducing the strain and accommodating the Si volume changes associated with the lithiation/delithiation electrochemical process. 32,47 The electrochemical performance of SnNPs in RGO was also investigated, which clearly demonstrates the advantages of the rapid synthesis method (Figure S10, Supporting Information). The performance of NPs in the RGO matrix can be optimized by varying the process conditions. More specifically, the RGO functional groups can be altered, and the specific hold time and synthesis temperature can control the NP size.

The rapid, in situ synthesis of nanoparticles via high-temperature radiative heating can be scaled up by three-dimensional (3D) printing. To prove the method's scalability, the RGO-SiMPs and RGO ribbons are fabricated using a 3D printer (Figure 5c, details in Figure S11 of Supporting Information). The 3D printed ribbons can be easily peeled off from the glass substrate to form freestanding and highly flexible electrodes (Figure 5c). For instance, the 3D printed GO

ribbon can be bent almost 180° with a tweezers, and the GO-Si ribbon can be wound into a spiral shape. To achieve scalable manufacturing of high-capacity nanoparticle anodes, a potential roll-to-roll setup can be envisioned where freestanding RGO-MPs composites with sufficient mechanical strength enter into the high-temperature thermal-shock zone for in situ synthesis of RGO-NPs. The thermal shock time (t=L/V) is determined by the length of the high temperature zone (L) and the roll-to-roll speed (V). Note that 5–15 nm SnNPs can be synthesized in a short time $(\sim 1 \text{ s})$, which demonstrates the potential of this method for commercial production (Figure S12, Supporting Information). The rapid, in situ high temperature thermal shock method via radiative heating opens up a new route for synthesizing a range of nanoparticle-based composites.

Conclusion. In summary, we have demonstrated an extremely simple and rapid process through high-temperature thermal radiation to synthesize high-capacity composite anodes with Si, Sn, and Al nanoparticles. The proposed synthesis method produced a high mass loading (>2.5 mg cm⁻²) of evenly distributed nanoparticles within the conductive RGO matrix without agglomeration. The in situ synthesis method can be adopted to many other metals, metal alloys, and semiconductors as well as insulator materials. The nanoparticle embedded RGO composites were successfully demonstrated as freestanding, carbon/binder-free high capacity LIB anodes. The enhanced cycling performance of the RGO-NPs film is due to the ultrafine particle sizes as well as the RGO matrix reducing the strain and accommodating the volume changes associated with the lithiation/delithiation process. Optimization of the in situ synthesis process can lead to further improvements in electrochemical performance. A fundamental understanding of the nanoparticle formation mechanism by thermal radiation, especially the role of defects in RGO, as well as the spatial and temporal distribution of temperature in the nonequilibrium process is under investigation through modeling and additional nanoscale studies.

ASSOCIATED CONTENT

S Supporting Information

The Supporting Information is available free of charge on the ACS Publications website at DOI: 10.1021/acs.nanolett.6b02096.

Experimental details for material synthesis and characterization, thermal shock process and characterization, and electrochemical and rheological property evaluations (PDF)

AUTHOR INFORMATION

Corresponding Author

*E-mail: binghu@umd.edu.

Author Contributions

Y.C. and Y.L. contributed equally.

Notes

The authors declare no competing financial interest.

ACKNOWLEDGMENTS

L.H. acknowledges the financial support from the Dean's office for the equipment setup. We acknowledge the support of the National Science Foundation #1635221. We acknowledge the support of the Maryland NanoCenter and its NispLab. Y.C. acknowledges the China Scholarship Council (CSC) for financial support.

REFERENCES

- (1) Lv, D.; Zheng, J.; Li, Q.; Xie, X.; Ferrara, S.; Nie, Z.; Mehdi, L. B.; Browning, N. D.; Zhang, J.-G.; Graff, G. L.; Liu, J.; Xiao, J. *Adv. Energy Mater.* **2015**, *5* (16), 1402290.
- (2) Jin, Y.; Zhang, S.; Zhu, B.; Tan, Y.; Hu, X.; Zong, L.; Zhu, J. Nano Lett. 2015, 15 (11), 7742–7747.
- (3) Ji, X.; Evers, S.; Black, R.; Nazar, L. F. Nat. Commun. 2011, 2, 325.
- (4) Ji, X.; Lee, K. T.; Nazar, L. F. Nat. Mater. 2009, 8 (6), 500-506.
- (5) Girishkumar, G.; McCloskey, B.; Luntz, A. C.; Swanson, S.; Wilcke, W. J. Phys. Chem. Lett. **2010**, 1 (14), 2193–2203.
- (6) Lu, J.; Jung Lee, Y.; Luo, X.; Chun Lau, K.; Asadi, M.; Wang, H.-H.; Brombosz, S.; Wen, J.; Zhai, D.; Chen, Z.; Miller, D. J.; Sub Jeong, Y.; Park, J.-B.; Zak Fang, Z.; Kumar, B.; Salehi-Khojin, A.; Sun, Y.-K.; Curtiss, L. A.; Amine, K. *Nature* **2016**, *529* (7586), 377–382.
- (7) Noh, M.; Kwon, Y.; Lee, H.; Cho, J.; Kim, Y.; Kim, M. G. Chem. Mater. 2005, 17 (8), 1926–1929.
- (8) Obrovac, M. N.; Chevrier, V. L. Chem. Rev. 2014, 114 (23), 11444-11502.
- (9) Lin, D.; Liu, Y.; Liang, Z.; Lee, H.-W.; Sun, J.; Wang, H.; Yan, K.; Xie, J.; Cui, Y. Nat. Nanotechnol. **2016**, 11, 626–632.
- (10) Lin, D.; Lu, Z.; Hsu, P.-C.; Lee, H. R.; Liu, N.; Zhao, J.; Wang, H.; Liu, C.; Cui, Y. *Energy Environ. Sci.* **2015**, 8 (8), 2371–2376.
- (11) Wang, H.; Yang, Y.; Liang, Y.; Robinson, J. T.; Li, Y.; Jackson, A.; Cui, Y.; Dai, H. *Nano Lett.* **2011**, *11* (7), 2644–2647.
- (12) Cui, L.-F.; Hu, L.; Choi, J. W.; Cui, Y. ACS Nano 2010, 4 (7), 3671-3678.
- (13) Zhou, X.; Yin, Y.-X.; Wan, L.-J.; Guo, Y.-G. Chem. Commun. 2012, 48 (16), 2198-2200.
- (14) Luo, J.; Zhao, X.; Wu, J.; Jang, H. D.; Kung, H. H.; Huang, J. J. Phys. Chem. Lett. **2012**, 3 (13), 1824–1829.
- (15) Lee, J. K.; Smith, K. B.; Hayner, C. M.; Kung, H. H. Chem. Commun. 2010, 46 (12), 2025–2027.
- (16) Zhou, M.; Li, X.; Wang, B.; Zhang, Y.; Ning, J.; Xiao, Z.; Zhang, X.; Chang, Y.; Zhi, L. Nano Lett. 2015, 15 (9), 6222–6228.
- (17) Ji, L.; Zhang, X. Energy Environ. Sci. 2010, 3 (1), 124-129.
- (18) Fu, K.; Yildiz, O.; Bhanushali, H.; Wang, Y.; Stano, K.; Xue, L.; Zhang, X.; Bradford, P. D. Adv. Mater. 2013, 25 (36), 5109-5114.
- (19) Xu, Y.; Zhu, Y.; Wang, C. J. Mater. Chem. A 2014, 2 (25), 9751–9757
- (20) Xu, Y.; Liu, Q.; Zhu, Y.; Liu, Y.; Langrock, A.; Zachariah, M. R.; Wang, C. Nano Lett. **2013**, 13 (2), 470–474.
- (21) Jung, S. C.; Choi, J. W.; Han, Y.-K. Nano Lett. 2012, 12 (10), 5342-5347
- (22) Su, X.; Wu, Q.; Li, J.; Xiao, X.; Lott, A.; Lu, W.; Sheldon, B. W.; Wu, J. Adv. Energy Mater. 2014, 4 (1), 1300882.
- (23) Liu, X. H.; Zhong, L.; Huang, S.; Mao, S. X.; Zhu, T.; Huang, J. Y. ACS Nano **2012**, 6 (2), 1522–1531.
- (24) Wang, C.; Wu, H.; Chen, Z.; McDowell, M. T.; Cui, Y.; Bao, Z. Nat. Chem. 2013, 5 (12), 1042–1048.
- (25) Kim, H.; Cho, J. Nano Lett. 2008, 8 (11), 3688-3691.
- (26) Deng, D.; Kim, M. G.; Lee, J. Y.; Cho, J. Energy Environ. Sci. 2009, 2 (8), 818.
- (27) Park, M.-H.; Kim, K.; Kim, J.; Cho, J. Adv. Mater. 2010, 22 (3), 415–418.
- (28) Liu, N.; Wu, H.; McDowell, M. T.; Yao, Y.; Wang, C.; Cui, Y. Nano Lett. 2012, 12 (6), 3315–3321.
- (29) Yao, Y.; McDowell, M. T.; Ryu, I.; Wu, H.; Liu, N.; Hu, L.; Nix, W. D.; Cui, Y. Nano Lett. **2011**, 11 (7), 2949–2954.
- (30) Wu, H.; Chan, G.; Choi, J. W.; Ryu, I.; Yao, Y.; McDowell, M. T.; Lee, S. W.; Jackson, A.; Yang, Y.; Hu, L.; Cui, Y. *Nat. Nanotechnol.* **2012**, *7* (5), 310–315.
- (31) Li, S.; Niu, J.; Zhao, Y. C.; So, K. P.; Wang, C.; Wang, C. A.; Li, J. Nat. Commun. **2015**, *6*, 7872.
- (32) Chan, C. K.; Peng, H.; Liu, G.; McIlwrath, K.; Zhang, X. F.; Huggins, R. A.; Cui, Y. Nat. Nanotechnol. 2008, 3 (1), 31–35.
- (33) Jin, Y.; Zhang, S.; Zhu, B.; Tan, Y.; Hu, X.; Zong, L.; Zhu, J. Nano Lett. 2015, 15 (11), 7742–7747.

(34) Zhu, B.; Jin, Y.; Tan, Y.; Zong, L.; Hu, Y.; Chen, L.; Chen, Y.; Zhang, Q.; Zhu, J. *Nano Lett.* **2015**, *15* (9), 5750–5754.

- (35) Zhu, Z.; Wang, S.; Du, J.; Jin, Q.; Zhang, T.; Cheng, F.; Chen, J. Nano Lett. **2014**, 14 (1), 153–157.
- (36) Zhou, X.; Wan, L.-J.; Guo, Y.-G. Adv. Mater. 2013, 25 (15), 2152-2157.
- (37) Mahmood, N.; Hou, Y. Adv. Sci. 2014, 1 (1), 1400012.
- (38) Wu, Z.-S.; Zhou, G.; Yin, L.-C.; Ren, W.; Li, F.; Cheng, H.-M. Nano Energy 2012, 1 (1), 107-131.
- (39) Bao, W.; Pickel, A. D.; Zhang, Q.; Chen, Y.; Yao, Y.; Wan, J.; Fu, K.; Wang, Y.; Dai, J.; Zhu, H.; Drew, D.; Fuhrer, M.; Dames, C.; Hu, L. Adv. Mater. 2016, 28 (23), 4684–4691.
- (40) Yao, Y.; Fu, K. K.; Yan, C.; Dai, J.; Chen, Y.; Wang, Y.; Zhang, B.; Hitz, E.; Hu, L. ACS Nano 2016, 10 (5), 5272-5279.
- (41) Chen, Y.; Fu, K.; Zhu, S.; Luo, W.; Wang, Y.; Li, Y.; Hitz, E.; Yao, Y.; Dai, J.; Wan, J.; Danner, V. A.; Li, T.; Hu, L. *Nano Lett.* **2016**, *16* (6), *3616–3623*.
- (42) Nair, R. R.; Blake, P.; Grigorenko, A. N.; Novoselov, K. S.; Booth, T. J.; Stauber, T.; Peres, N. M. R.; Geim, A. K. Science 2008, 320 (5881), 1308–1308.
- (43) Li, J.; Dahn, J. R. J. Electrochem. Soc. 2007, 154 (3), A156-A161.
- (44) Obrovac, M. N.; Krause, L. J. J. Electrochem. Soc. 2007, 154 (2), A103-A108.
- (45) Hatchard, T. D.; Dahn, J. R. J. Electrochem. Soc. **2004**, 151 (6), A838–A842.
- (46) Andreas Netz, R. A. H. J. Power Sources 2003, 119, 95-100.
- (47) Kim, H.; Seo, M.; Park, M.-H.; Cho, J. Angew. Chem., Int. Ed. **2010**, 49 (12), 2146–2149.